Available online at www.sciencedirect.com

ScienceDirect

Solar Energy 117 (2015) 1–9

SOLAR ENERGY

www.elsevier.com/locate/solener

Zinc oxide–nickel cermet selective coatings obtained by sequential electrodeposition

N.P. Klochko [a], K.S. Klepikova [a], I.I. Tyukhov [b,*], Y.O. Myagchenko [c], E.E. Melnychuk [c], V.R. Kopach [a], G.S. Khrypunov [a], V.M. Lyubov [a], A.V. Kopach [a], V.V. Starikov [a], M.V. Kirichenko [a]

[a] National Technical University "Kharkiv Polytechnic Institute", 21, Frunze str., 61002 Kharkiv, Ukraine
[b] All-Russian Research Institute for Electrification of Agriculture (VIESH), 2, 1-st Veschnyakovsky proezd, 109456 Moscow, Russian Federation
[c] National Taras Shevchenko University, 62, Volodymyrska str., 03680 Kyiv, Ukraine

Received 14 February 2015; received in revised form 28 March 2015; accepted 31 March 2015

Communicated by: Associate Editor Takhir M. Razykov

Abstract

The investigation of pulse electrodepositing modes influence on crystal structure, morphology and optical properties of ZnO has revealed the conditions in which quasi-one-dimensional (1D) ZnO nanorod arrays are formed as separate nanorods. Due to a sufficiently high resistance of zinc oxide, the electrodeposition of nickel on the fluorine doped tin oxide (FTO)/ZnO surfaces carried out in space between the ZnO nanorods. An incomplete filling of the gaps between nanorods by the nickel nanoparticles through subsequent Ni electrodeposition ensured the creation of ZnO–Ni graded cermets. The cermets, in which electrochemical filling of the spaces between ZnO nanorods by Ni, was performed in the pulse mode. It provided higher absorption of visible and near IR light. It was shown that the manufactured ZnO–Ni graded cermets have high light absorption combined with comparatively low thermal losses, so these cermets are promising cheap and affordable selective coatings for solar heat collectors.

© 2015 Elsevier Ltd. All rights reserved.

Keywords: Pulse electrodeposition; Cermet; Nickel; Zinc oxide; Selective coating

1. Introduction

The efficiency of solar energy conversion into heat is mainly determined by the optical properties of an absorber surface. The efficient selective solar absorber surface should have the good optical properties, i.e. high absorption A_s over the spectral range of solar spectrum (0.3–2.5 μm) combined with low thermal losses ε because of re-radiation at longer wavelengths (beyond 2.5 μm). Several solar absorber materials based on cermets have been reported by various authors (Grainghead et al., 1979; Klochko et al., 2005; Cheng et al., 2013; Nuru et al., 2014; Li et al., 2012; Nuru et al., 2015; Feng et al., 2015). The highly absorbing cermet coatings (metal-dielectric composites), consist of metal or carbon particles in a dielectric matrix. The other cermets are the porous oxides impregnated with metals. These coatings are transparent in the thermal infrared region and they are strongly absorbing in the solar spectrum region because of the interband transitions in the metal and the small

---

* Corresponding author at: UNESCO Chair, the All-Russian Research Institute for Electrification of Agriculture (VIESH), 2, 1-st Veschnyakovsky proezd, 109456 Moscow, Russian Federation. Tel.: +7 (499) 171 05 23/171 19 20; fax: +7 (499) 170 51 01.
E-mail addresses: viesh@dol.ru, ityukhov@yahoo.com (I.I. Tyukhov).
URL: http://www.viesh.ru/ (I.I. Tyukhov).

http://dx.doi.org/10.1016/j.solener.2015.03.047
0038-092X/© 2015 Elsevier Ltd. All rights reserved.

particle resonance. A variety of techniques, such as magnetron sputtering (Cheng et al., 2013; Feng et al., 2015), electron-beam evaporation (Nuru et al., 2014, 2015), sol–gel technique (Katumba et al., 2008), electroplating (Klochko et al., 2005), coating by the aqueous solution-chemical method (Li et al., 2012), metal pigmentation of anodically oxidized porous surfaces (Kadirgan et al., 1999) can produce the composite coatings. The absorbing cermet layer may have either uniform or graded metal (or carbon) content. Early (Katumba et al., 2008) cermet selective surfaces for solar thermal collectors were prepared by uniform dispersion of 55–62 nm carbon nanoparticles in zinc oxide (ZnO) matrices. Guided by the double interference absorption theory (Grainghead et al., 1979) in the graded cermet, the reflectance from the cermet is reduced by gradually increasing the metal volume fractions; hence the refractive index decreases as a function of depth from the surface to the base of the film. So, it provides improved absorption of visible light due to the additional antireflection effect caused by the graded refractive index profile. Graded metal-pigmented alumina selective coatings are used. As a rule, oxide coatings were obtained by anodization of aluminum. The oxide coating was the porous alumina layer whose pores are perpendicular to the aluminum substrate and coating was partly impregnated with Ni, V, Cr, Co, Cu, Mo, Ag, or W in form rod-like particles 30–50 nm in diameter. The high visible absorptance of the cermet is both intrinsic and also geometrically enhanced, since typical structure of this coating from surface to substrate consists of the antireflection layer composed of a transparent oxide material that enhances solar absorption, a low metal volume fraction cermet solar absorbing layer and a high metal volume fraction cermet solar absorber layer (Cheng et al., 2013).

Zinc oxide, which proved to be successful component of the cermet selective coatings for solar thermal collectors (Katumba et al., 2008) is a promising widespread inexpensive material with high resistivity in its intrinsic form. ZnO is the wide bandgap semiconductor with a direct bandgap of about 3.37 eV. It has attracted increasing interest due to its unique ability to form a variety of nanostructures. A special attention is focused on the ZnO in the form one-dimensional (1D) nanorod arrays vertically arranged with respect to the substrate. The ordered 1D ZnO nanostructures are successfully manufactured by various methods and already used in various technologically important devices such as short-wavelength lasers, electroluminescent devices, sensors, photocatalytic systems and third generation of solar cells (Skompska and Zarębska, 2014). Electrochemical deposition has a high potential due to a more efficient material consumption and reduces investment costs as compared to production techniques involving high vacuum technologies (Yantara et al., 2012; Sokol et al., 2014). The pulse electrodeposition has a number of additional advantages because the preferred orientation of ZnO films and their morphology may be controlled by changing such pulse parameters like the cathodic average current density or cathode on/off potentials, the pulse length (pulse on-time), the pulse shape and the pulse period. These parameters can be changed independently over wide ranges in contrast to the direct current plating or potentiostatic electrolysis. Early (Klochko et al., 2014) it was optimized the pulse electrodeposition conditions for the fabrication of antireflective 1D ZnO coatings with parabolic nanonipples, which demonstrated the moth-eye effect. Since pulse plating can produce 1D ZnO nanostructured antireflective arrays (Klochko et al., 2012; Sokol et al., 2014; Klochko et al., 2014), in this work for the first time it was investigated the possibility of creating the graded cermet selective coatings using two sequential processes of electrochemical deposition, namely, electrodeposition of nickel nanoparticles in the spaces between previously electrodeposited ZnO nanorods. It should be noted that for this the electrodeposited zinc oxide must have sufficiently large resistivity and has to be in the form the array of separate 1D ZnO. So, the purpose of this work was to investigate the crystal structure, morphology, optical and electrical properties of the pulse electrodeposited ZnO arrays and to study the influence of Ni potentiostatic and pulse plating modes on structure, optical properties, morphology and optical selectivity of graded ZnO–Ni cermets obtained by successive ZnO and Ni electrodeposition in order to create cheap and affordable selective coatings for solar heat collectors.

2. Experimental procedures

Zinc oxide arrays were obtained by cathodic electrochemical deposition using a three-electrode electrochemical scheme with not stirred aqueous electrolyte containing 0.01 M $Zn(NO_3)_2$ and 0.1 M $NaNO_3$ on the SnO_2:F/glass cathode substrates (FTO, TEC 7 Pilkington Company, USA). Both potentiostatic and pulse plating modes of ZnO operation were realized in the standard thermostatic three-electrode electrochemical cell by using platinum spring as counter-electrode and saturated Ag/AgCl reference electrode. The pulse plating mode for the ZnO nanorods electrodeposition was performed by applying rectangular potential pulses, so that the lower and upper potential limits were, respectively, U_{off} and U_{on} (Table 1). The values of cathode potentials provided by a programmable impulse potentiostat PI-0.5–1.1 were measured vs. Ag/AgCl electrode. According to Skompska and Zarębska (2014) the seeding stage in general enhances formation of the vertically aligned ZnO nanorods and allows controlling their diameter and density in electrochemical deposition. So, in a first electrodeposition step in some cases ZnO seed layers were formed by potentiostatic electrochemical deposition in the same electrolyte during short time $\tau = 30$ s at potential $U = -1.3$ V. After that the pulse plating of ZnO nanorods was carried out during time τ (Table 1). A duty cycle (Dc) was given as relation $T_{on}/(T_{on} + T_{off})$, where T_{on} is a time at potential U_{on} and T_{off} is a time at potential U_{off}. Potential pulse frequency f

Table 1
Electrodeposition parameters of pulse plated ZnO arrays.

Specimen		Electrodeposition mode						
		FTO substrate potential (V)			Dc	f (Hz)	t (°C)	τ (s)
		U_{on}	U_{off}	U				
ZnO68		–1.4	–0.8	–	0.4	2	70	600
	Seed	–	–	–1.3	–	–	70	30
ZnOS5		–1.3	–0.7	–	0.4	2	70	1800
ZnOS19								600
ZnOS20								600

defined as the reciprocal of the cycle time ($T_{on} + T_{off}$) was 2 Hz (Table 1).

Electrodeposition of nickel on the smooth surface of FTO transparent conductive substrates and on the electrodeposited ZnO arrays (FTO/ZnO substrates) was performed in a widely used Watts electrolyte, containing 330 g/l $NiSO_4 \cdot 7H_2O$, 55 g/l $NiCl_2 \cdot 6H_2O$ and 40 g/l·H_3BO_3 (pH 5.5) using programmable impulse potentiostat PI-50–1.1. It was in the same three-electrode electrochemical cell, but with large nickel plate as counter-electrode in potentiostatic and pulse modes listed in Table 2.

The conventional hot probe characterization method was used for the determination of a semiconductor type in accordance with Axelevitch and Golan (2013). The ohmic indium contacts to ZnO were created to study the electrical properties of the electrodeposited zinc oxide nanorods through dark current–voltage (*I–V*) characteristics. To prevent short circuits, the In contact vacuum deposition was performed at 70° angle from the normal to the FTO/ZnO substrate in the separate locations of the ZnO and FTO areas using a removable shadow mask made of aluminum. Then, a conductive adhesive with silver powder filler "Kontaktol" was applied on the indium surface and copper microwires were bonded thereto through the thin adhesive layer.

The prepared test sample FTO/ZnO/In/"Kontaktol"/Cu was used for the measurements of dark *I–V* characteristics that were measured under the curve tracer scheme (Mazda, 1987), namely the test sample was connected to the industrial curve tracer L2-56 for direct visualization of *I–V* curve of the test specimen on the screen. Idealized scheme of the FTO/ZnO/In/"Kontaktol"/Cu test sample is shown in Fig. 1a. On the base of total resistance $R_t = U/I$ obtained from the *I–V* curve between two contacts, which both are applied to FTO, it is possible to calculate the FTO resistivity ρ_{FTO}:

$$\rho_{FTO} = R_t \cdot S_{FTO}/w, \tag{1}$$

where S_{FTO} is the product of the slit length and the SnO_2:F film thickness; w is the distance between two In contacts (the slit width).

As calculated according to the *I–V* curve, $\rho_{FTO} = 3.5 \times 10^{-4}$ Ohm cm that corresponds to certificate data for FTO 7 TEC Pilkington Company, USA. The calculations of resistivity of the zinc oxide nanorods ρ_{ZnO} were based on *I–V* measurements for the contacts between the upper ends of the zinc oxide nanorods and FTO:

$$U/I = R_\Sigma = \rho_{FTO} \cdot L/S_{FTO} + 2 \cdot \rho_{ZnO} \cdot t/S_c, \tag{2}$$

where R_Σ is total resistance obtained from the *I–V* data between two In contacts, one of which is applied to FTO and another is located on the upper ends of the zinc oxide nanorods; L is slit width for these contacts; t is average length of the ZnO nanorod, obtained in accordance with Klochko et al. (2015); S_c is area of the In contact; factor 2 was applied to take into account a total area of voids between the ZnO nanorods.

If both contacts were applied between the upper ends of the zinc oxide nanorods, the ratio U/I corresponds to the expression:

$$U/I = R_\Sigma = \rho_{FTO} \cdot l/S_{FTO} + 4\rho_{ZnO} \cdot t/S_c, \tag{3}$$

where l is clearance between the centers of indium contacts.

Table 2
Parameters of nickel electrodeposition.

Specimen	The sequence of layers of the sample	Ni electrodeposition mode					
		Substrate potential (V)			Dc	f (Hz)	τ (s)
		U_{on}	U_{off}	U			
ZnO68Ni2	FTO/ZnO68/Ni	–	–	−1.15	–	–	120
Ni5	FTO/Ni	–	–	−1.3	–	–	300
ZnOS19.3Ni	FTO/ZnOS19/Ni	–	–	−1.1	–	–	60
ZnOS19.4Ni	FTO/ZnOS19/Ni	−1.1	−0.5	–	0.4	2	150
ZnOS20.2Ni	FTO/ZnOS20/Ni	–	–	−0.8	–	–	150
ZnOS20Ni–0.8	FTO/ZnOS20/Ni	–	–	−0.8	–	–	150
ZnOS20.4Ni	FTO/ZnOS20/Ni	−0.8	−0.5	–	0.4	2	375

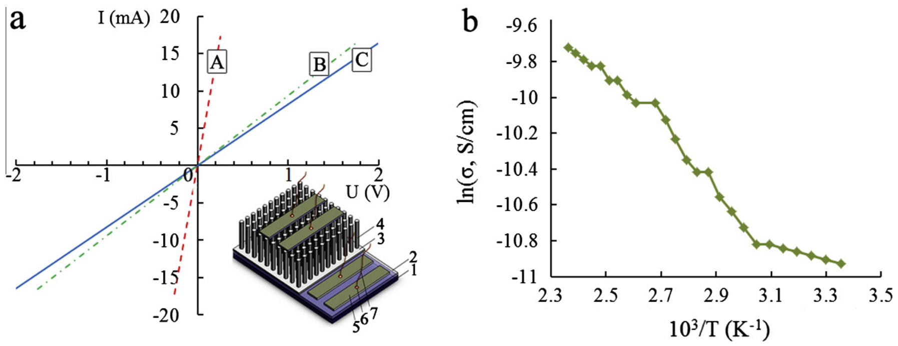

Fig. 1. (a) Idealized scheme of the FTO/ZnO/In/“Kontaktol”/Cu appliance: 1 – glass; 2 – FTO; 3 – ZnO seed layer; 4 – ZnO nanorod; 5 – Indium contact coated by “Kontaktol”; 6 – copper wire attaching point; 7 – copper wire; (b) *I–V* curves: 1 – both contacts are applied to FTO; 2 – one contact is applied to FTO and another one is located on the upper ends of the zinc oxide nanorods; 3 – both contacts are applied between the upper ends of the zinc oxide nanorods; (c) results of measurements of activation energies of the electrodeposited ZnO arrays.

After above mentioned analytical processing of dark *I–V* characteristics obtained for the test sample during its cooling in air from 150 °C to 25 °C activation energies E_a of the ZnO arrays electrical conduction were estimated in accordance with Prasada Rao and Santhoshkumar (2009) using coordinates $\ln\sigma$ versus $10^3/T$ (Fig. 1c), where $\sigma = 1/\rho_{\text{ZnO}}$ is ZnO conductivity, and T is absolute temperature.

The optical properties of the zinc oxide layers and of the electrodeposited ZnO–Ni graded cermets were studied with an “SF-2000“ spectrophotometer equipped with an “SFO-2000“ mirror and diffuse reflectance accessory. FTO substrates served as control samples when the optical transmission spectra $T(\lambda)$ were recorded. The optical band gap E_g of the ZnO layers was determined as described by Klochko et al. (2012) through extrapolation of the linear portion of the $[-\ln(T)\cdot h\nu]^2$ dependence on $h\nu$ (the energy axis). The structural disorder of the electrodeposited zinc oxide layers was assessed by the Urbach energy E_o determined from the slope of the linear portion of the $\ln[-\ln(T)]$ dependence on $h\nu$. Spectra of diffuse reflectance $R_d(\lambda)$ and mirror reflectance $R_s(\lambda)$ were measured at light incidence angle $\vartheta = 8°$ relative to the normal to the surface. Total reflectance R was calculated as sum of R_d and R_s.

Optical properties of the electrodeposited ZnO–Ni cermet specimens were additionally analyzed by means of photometer “FM-59“, that allowed to determinate integrated optical absorption A_s in the range of wave lengths $0.3\ \mu m \leqslant \lambda \leqslant 2.4\ \mu m$, and by thermoradiometer TRM “I” measured emittance ε in the range of wavelengths $4\ \mu m \leqslant \lambda \leqslant 40\ \mu m$.

To analyze phase compositions of the cermets as well as structural and substructural parameters of the ZnO arrays and Ni nanoparticles, we recorded X-ray diffraction patterns (XRD) by a “DRON-4” diffractometer with Co Kα radiation ($\lambda = 1.7889$ Å). Scanning was performed with Bragg–Brentano focusing (theta – 2 theta). The resulting X-ray diffraction patterns were processed (exclusion of the background, separation of the $K_{\alpha 1} - K_{\alpha 2}$ doublet, etc.), and the profile parameters of the diffraction lines were calculated by “New-Profile v.3.4 (486)” and “OriginPro v.7.5” software. The presence of crystalline phases was revealed by comparing the experimental diffraction patterns with the reference database JCPDS with the use of PCPDFWIN v.1.30 software. The sizes of the coherent-scattering regions (CSRs) in ZnO arrays and microstrains $\Delta d/d$ (where d is the crystal lattice constant according to JCPDS, and Δd is the difference between the experimental and reference lattice constants) in zinc oxide and in Ni nanoparticles were estimated by analyzing the broadening of the X-ray diffraction peaks, with instrumental broadening taken into account, by the method of Williamson–Hall approximations (Palatnik, 1983; Tsybulya and Cherepanova, 2008; Zak et al., 2011). The crystal lattice constants a and c of the hexagonal zinc oxide phase were calculated from the positions of the last two indexed lines in the X-ray diffraction patterns by the Nelson–Reilly graphical extrapolation method and refined using the least-squares method (LSM) by UnitCell software on the basis of all recorded reflections in the X-ray diffraction patterns (Palatnik, 1983; Tsybulya and Cherepanova, 2008). The average grain size (D) of the electrodeposited Ni nanoparticles in the cermets were estimated in accordance with Zak et al. (2011) by the X-ray line broadening method using the Scherrer equation: $D = (k\lambda/B_D\cos\theta)$, where D is the particle size in nanometers, λ is the wavelength of the Co Ka radiation, k is a constant equal to 0.94, B_D is the peak width at half-maximum intensity and θ is the peak position. The residual stresses in the ZnO arrays were calculated from the lattice constants of the electrodeposited and reference samples by using the elasticity constants of the material in various directions (Tsybulya and Cherepanova, 2008). To study the texture of the electrodeposited zinc oxide arrays, the integrated intensities of the X-ray diffraction peaks in accordance with Palatnik (1983) were investigated by the Harris method. For each peak, it was calculated the pole density $P(hkl)$, which characterizes the probability with which the normal to the crystallite surface coincides with that to the (hkl) plane, i.e., determines the number of crystallites in which the ($h\,k\,l$) planes are parallel to the sample surface. The pole densities were found for all recorded X-ray diffraction peaks; the values $P(h\,k\,l) \gg 1$ were assigned to the texture axes.

The surface morphology of the zinc oxide arrays and of the electrodeposited ZnO–Ni cermets was studied by intermittent contact atomic force microscopy (AFM) using a “Nano-Laboratoriya Integra Prima NT-MDT” setup. Processing of the AFM images was carried out using the software “Nova v.1.0.26 Build 1452 (NT-MDT)” and software module “Image Analysis”.

3. Results and discussion

The study concerning evaluation of electrical conductivity of the nanostructured zinc oxide arrays was conducted by means of dark current–voltage characteristics using the test sample. The idealized scheme of the FTO/ZnO/In/“Kontaktol”/Cu appliance is shown in Fig. 1a. It has revealed that all obtained I–V curves were linear and symmetric (Fig. 1b) that confirmed the ohmic properties of the prepared In contacts. As it was revealed by hot probe measurements, the zinc oxide arrays had n-type conductivity, and according to I–V data they had high resistivity. For example, the calculated resistivity ρ_{ZnO} for ZnOS5 (specimen) was 5.5×10^4 Ohm cm, i.e. it was by eight orders of magnitude higher than the value of the electrical resistivity of the FTO substrate ρ_{FTO}. Estimation of activation energy E_a of the electrodeposited arrays of 1.1 μm length ZnO nanorods (ZnOS5 specimen) has shown (Fig. 1c) comparatively slight increase in ZnO conductivity upon heating. $E_a \approx 0.14$ eV and $E_a \approx 0.03$ eV values were obtained for the first cooling. In repeated experiments with ZnO heating up to 150 °C we noted an additional increase in their resistivity after cooling, which consistent to the fundamentals of zinc oxide (Janotti and Van de Walle, 2009). On the whole, the studies of the electrical properties have shown that due to a sufficiently high resistance of the zinc oxide the electrodeposition of nickel on the FTO/ZnO surfaces must be carried out in those areas where the thickness of the zinc oxide layer is minimal, i.e. in between the ZnO nanorods. So, an incomplete filling of the gaps between nanorods by the nickel nanoparticles, in our opinion, should ensure the creation of ZnO–Ni graded cermets.

In principle, to identify opportunities of the electrodeposition in Watts electrolyte of nickel nanoparticles into the spaces between the nanoprotrusions of the electrodeposited zinc oxide layers on FTO to form nanocomposites it was used specimen ZnO68 that was obtained without any seed layers (Table 1) and therefore it has represented the array of randomly located accreted ZnO nanocrystals. Fig. 2a shows three-dimensional image of ZnO68 obtained by atomic force microscopy. Table 2 represents the mode of ZnO68Ni2 specimen creation by means of Ni potentiostatic electrodeposition on the ZnO68 surface. If Ni electrodeposited on the smooth FTO surface (Ni5 specimen in Table 2) it produced a smooth continuous film, which is presented as AFM picture in Fig. 2b. Fig. 2c demonstrates a sleek microprofile of the nickel on the flat FTO surface in the Ni5 specimen. Because nickel Watts electrolyte has pH 5.5, the dissolution of the ZnO during Ni electrodeposition did not occur that was proving by X-ray diffraction pattern of ZnO68Ni2 specimen (Fig. 3a) as well as by the results of ZnO68Ni2 optical studies, which are shown in Figs. 3b and 4. Structure analysis of XRD pattern of ZnO68Ni2 nanocomposite has revealed that along with diffraction peaks of zinc oxide of hexagonal modification (JCPDS no. 36-1451). It was registered only one weak diffraction peak of nickel, which corresponds to a cubic system (JCPDS no. 04-0850). In our opinion, the latter is explained by a small amount of nickel in ZnO68Ni2 composition. Analysis of the peak of Ni (1 1 1) by using the Scherer equation showed that the average diameter of the nickel nanoparticles $D \approx 80$ nm. Microstrains $\Delta d/d$ in Ni nanoparticles are 1.7×10^{-3} arbitrary units (Table 3). Our calculations showed that electrodeposited ZnO array was fine-crystalline (its CSRs do not exceed hundreds of nanometers), characterized by slightly increased lattice parameters a compared to the reference ZnO (according to JCPDS no. 36-1451, $a = 3.250$ Å, $c = 5.207$ Å) and has minor compression microstrains. The residual stresses in the ZnO

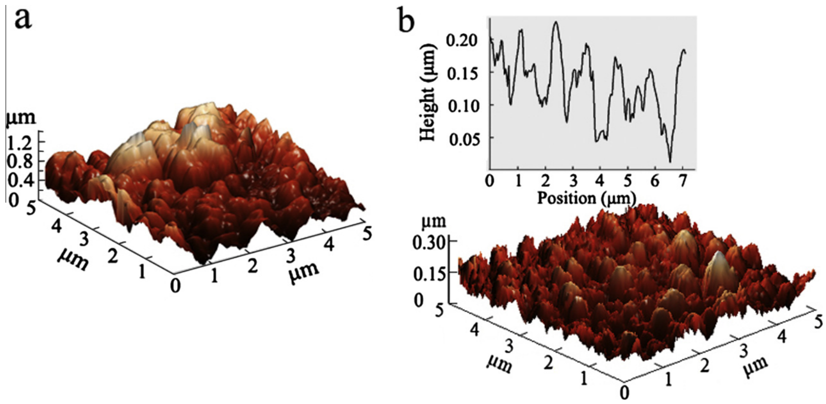

Fig. 2. (a) Three-dimensional image of the specimen ZnO68; (b) three-dimensional image of the nickel film on the surface of FTO (specimen Ni5); (c) microprofile of Ni5 according to the AFM.

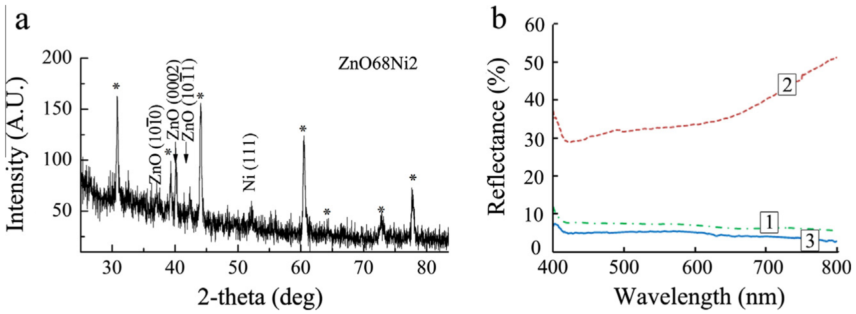

Fig. 3. (a) X-ray diffraction of ZnO68Ni2 nanocomposite that was obtained by electrochemical deposition of nickel nanoparticles over ZnO68 specimen; (b) total reflectance spectra: 1 – ZnO68; 2 – Ni5; 3 – ZnO68Ni2.

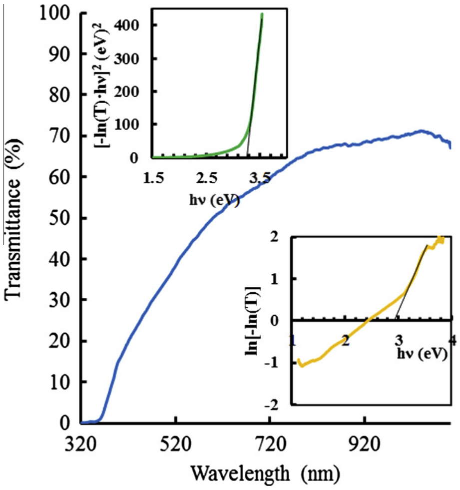

Fig. 4. (a) Transmittance spectra of ZnO68Ni2; (b) and (c) dependences for determining of optical band gap E_g and Urbach energy E_o, respectively.

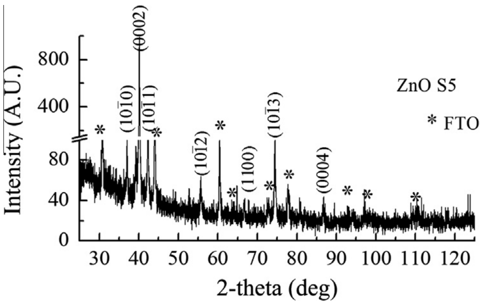

Fig. 5. X-ray diffraction of the nanostructured zinc oxide array ZnOS5 electrodeposited on FTO substrate.

arrays were 0.45 GPa. The ZnO68Ni2 specimen has slight vertical preferential orientation of ZnO with *c* axis perpendicular to the substrate ($P_{002} = 2.59$) and therefore it does not form the array of nanorods, which is also confirmed by Fig. 2a.

As can be seen in Fig. 3b, the smooth nickel film on FTO (Ni5 specimen) has the highest reflectance in the visible (mainly the mirror reflectance $R_s(\lambda)$, as shown by our measurements). The total optical reflectance of ZnO68Ni2 nanocomposite is lower than $R(\lambda)$ of the nanostructured zinc oxide array ZnO68 or nickel film on the FTO surface. However, as shown in Fig. 4a, the ZnO68Ni2 nanocomposite quite well transmits light, probably because of the small amount of nickel in its composition. Other optical properties of ZnO68Ni2 nanocomposite such as bandgap $E_g = 3.26$ eV and Urbach energy $E_o = 0.12$ eV were obtained using graphical dependencies in Fig. 4a and b, respectively, which are typical for the electrodeposited nanostructured arrays of zinc oxide (Klochko et al., 2012; Sokol et al., 2014; Klochko et al., 2014, 2015).

Probable cause of small filling in ZnO68Ni2 of the space within the zinc oxide array with the nickel nanoparticles is the significant density of ZnO68 zinc oxide nanostructure, while for the creation of the graded cermet nanocomposites, as we have seen, needs to have separate ZnO nanorods grown perpendicular to the substrate. Therefore, further experiments concerning formation of nanocomposites were conducted with arrays of zinc oxide nanorods well textured in the ⟨001⟩, which were deposited with creation of ZnO seed layers in the first electrodeposition step.

Fig. 5 demonstrates X-ray diffraction pattern of the nanostructured zinc oxide array ZnOS5, which was electrodeposited using seed layer, and Table 4 shows its

Table 3
Structural parameters of components of ZnO68Ni2 nanocomposite.

Specimen ZnO68Ni2	CSR (nm)	*D* (nm)	$\Delta d/d \cdot 10^{-3}$	Residual stresses (GPa)	Lattice parameters (Å)				Texture	
					Nelson–Reilly method		LSM		P_{hkl}	*h k l*
					a	*c*	*a*	*c*		
ZnO	90–200	–	1.1–1.9	0.45	3.288	5.174	3.269	5.196	2.59	(0 0 2)
Ni	–	80	1.7	–	–	–	–	–	–	–

Table 4
Structural parameters of the ZnOS5 nanostructured zinc oxide array electrodeposited using seed layer.

Specimen ZnOS5	CSR (nm)	$\Delta d/d \cdot 10^{-3}$	Residual stresses (GPa)	Lattice parameters (Å)				Texture	
				Nelson–Reilly method		LSM		P_{hkl}	*h k l*
				a	*c*	*a*	*c*		
ZnO	80–200	0.1–0.7	−0.36	3.254	5.217	3.256	5.214	3.24	(002)

structural parameters. Investigation of the ZnOS5 structure shown that this zinc oxide array differs from ZnO68 above all by quite perfect texture in the ⟨001⟩, which is characteristic for nanorods that grow perpendicular to the substrate.

Fig. 6a shows the results of the study of optical properties of nanostructured zinc oxide arrays of ZnOS19 series obtained in the same mode as the ZnOS5, but in a shorter time, namely, by pulse plating with creation of ZnO seed layers in the first electrodeposition step (Table 1). Fig. 6b demonstrates transmittance $T(\lambda)$ and reflection $R(\lambda)$ spectra of ZnOS19.3Ni and ZnOS19.4Ni cermets based on them (Table 2). One can see that the zinc oxide arrays of ZnOS19 series were quite transparent, their optical reflectance in the visible range was about 5% and little changed after electrodeposition of nickel nanoparticles and formation ZnOS19.3Ni and ZnOS19.4Ni graded cermets. Despite transparency of the ZnOS19 series films, ZnOS19.3Ni and ZnOS19.4Ni cermets based on them were almost opaque to visible light.

Fig. 7 demonstrates AFM data concerning surface morphology of ZnOS19.3Ni and ZnOS19.4Ni cermets. It can be seen in their three-dimensional images (Fig. 7a and c) that both samples have surface morphology characteristic for the one-dimensional arrays. The space between nanorods is not completely filled with nickel that is evidenced by

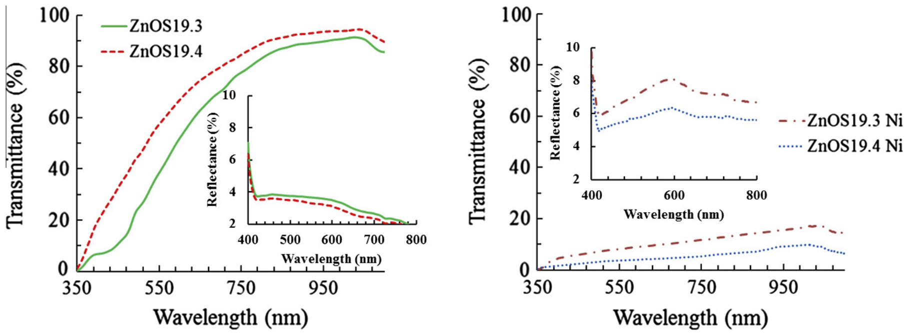

Fig. 6. (a) Transmittance $T(\lambda)$ and the reflection $R(\lambda)$ spectra of ZnOS19.3 and ZnOS19.4 nanostructured ZnO arrays obtained by pulse plating with creation of ZnO seed layers in the first electrodeposition step; (b) transmittance $T(\lambda)$ and the reflection $R(\lambda)$ spectra of ZnOS19.3Ni and ZnOS19.4 Ni graded cermets.

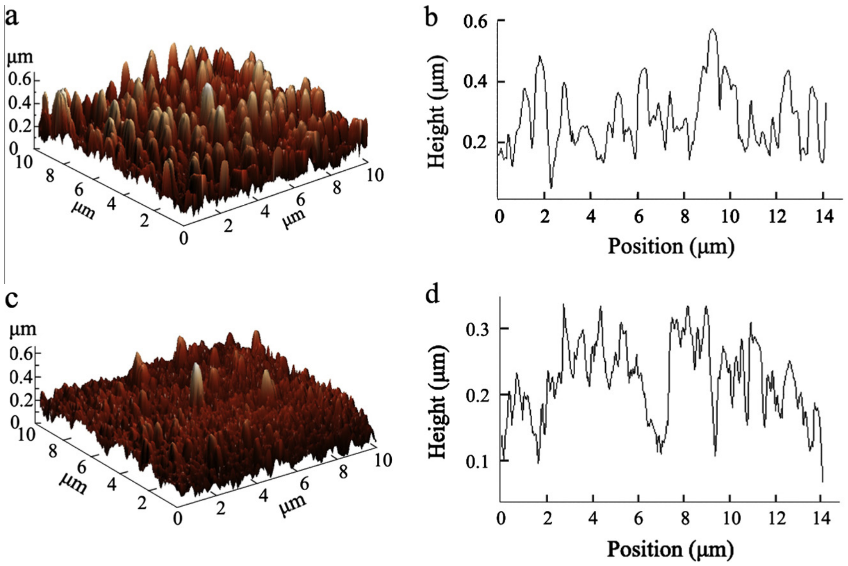

Fig. 7. (a) and (c) Three-dimensional images of ZnOS19.3Ni and ZnOS19.4Ni graded cermets, respectively; (b) and (d) the relevant microprofiles of ZnOS19.3Ni and ZnOS19.4Ni, respectively, according to the AFM.

Table 5
Integrated optical absorptions A_s and infrared emittances ε of ZnO–Ni graded cermets obtained by consistent electrodepositions as shown in Tables 1 and 2.

Specimen	A_s (%)	ε (%)
ZnOS20.2Ni	85	25
ZnOS20Ni–0.8	92	28
ZnOS20.4Ni	83	14

their microprofiles (Fig. 7b and d). These 1D ZnO arrays have tops of parabolic shape not plated with nickel, which must demonstrate the moth-eye antireflective effect (Klochko et al., 2012; Sokol et al., 2014; Klochko et al., 2014). As shown in Fig. 7c and d, ZnOS19.4Ni cermet, in which electrochemical filling of the spaces between electrodeposited ZnO nanorods by Ni was performed in the pulse mode (Table 2) have more densely filled with nickel nanoparticles gaps between the nanorods of zinc oxide, although according to the time τ of the electrodeposition, in view of the *Dc*, the electric charges spent on the manufacture of these samples were the same. According to Fig. 6b, as compared with ZnOS19.3Ni obtained by potentiostatic Ni plating, the ZnOS19.4Ni graded cermet prepared by pulse Ni electrodeposition within 1D ZnO arrays has lower transmittance and reflection in the visible range and therefore better absorb solar light.

Graded cermet specimens ZnOS20.2Ni, ZnOS20Ni–0.8 and ZnOS20.4Ni with increased areas were obtained on the base of ZnOS20 1D zinc oxide array electrodeposited in the same mode as ZnOS19, namely, by pulse plating with creation of ZnO seed layers in the first electrodeposition step (Table 1) and by the consistent Ni electrodeposition (Table 2). X-ray diffraction analysis of these cermets has revealed the increasing of intensities of Ni (111) and Ni (222) reflections relative to the ZnO peaks, indicating an increase in the nickel content in the compositions of these cermets as compared with ZnO68Ni2. Analysis by using the Scherer equation showed that the average diameters of the nickel nanoparticles $D \approx 70\text{–}115$ nm. Microstrains $\Delta d/d$ in Ni nanoparticles are $(1\text{–}1.6) \times 10^{-3}$ arbitrary units if the nickel electrodeposition was performed in potentiostatic modes. When Ni was pulse plated, the microstrains of its nanoparticles were much greater $\Delta d/d = 1.1 \times 10^{-2}$ (arbitrary units).

Table 5 shows data for integrated optical absorptions A_s and infrared emittances ε of some graded ZnO–Ni cermets obtained by consistent electrodeposition confirming that due to high visible absorption combined with comparatively low thermal losses ε these cermets are promising selective coating. After additional optimization of the nickel pulse electrodeposition parameters it can be used in solar heat collectors.

4. Conclusions

The investigation of influence of pulse electrodeposition modes with or without creation of ZnO seed layers in the first electrodeposition step on crystal structure, on morphology and optical properties of ZnO has revealed the conditions in which 1D ZnO arrays were formed as separate nanorods. The research of the ZnO electrical properties has shown its high resistivity comparatively to fluorine doped tin oxide (FTO) substrate and slight increasing in the ZnO conductivity upon heating. Due to the sufficiently high resistance of the zinc oxide the electrodeposition of nickel on the FTO/ZnO surfaces carried out in those areas where the thickness of the zinc oxide layer is minimal, i.e. in between the ZnO nanorods. An incomplete filling of the gaps between nanorods by the nickel nanoparticles through subsequent Ni electrodeposition ensured the creation of ZnO–Ni graded cermets. As studies have shown, the 1D ZnO arrays have tops of parabolic shape not plated with nickel that demonstrate the moth-eye antireflective effect. The cermets, in which electrochemical filling of the spaces between ZnO nanorods with Ni was performed in the pulse mode, have more densely filled with nickel gaps between 1D ZnO, that provides higher absorption of visible light. It was shown that the manufactured ZnO–Ni graded cermets obtained by consistent electrodeposition of 1D ZnO nanostructured arrays and nickel nanoparticles have high visible absorption combined with comparatively low thermal losses, so they are promising cheap and affordable selective coating for solar heat collectors.

References

Axelevitch, A., Golan, G., 2013. Hot-probe method for evaluation of majority charged carriers concentration in semiconductor thin films. Facta Univ. Ser.: Electron. Energ. 26, 187–195.

Cheng, J., Wanga, C., Wanga, W., Dua, X., Liu, Y., Xue, Y., Wanga, T., Chen, B., 2013. Improvement of thermal stability in the solar selective absorbing Mo–Al_2O_3 coating. Sol. Energy Mater. Sol. Cells 109, 204–208.

Feng, J., Zhang, S., Lu, Y., Yu, H., Kang, L., Wang, X., Liu, Z., Ding, H., Tian, Y., Ouyang, J., 2015. The spectral selective absorbing characteristics and thermal stability of SS/TiAlN/TiAlSiN/Si_3N_4 tandem absorber prepared by magnetron sputtering. Sol. Energy 111, 350–356.

Grainghead, H.D., Bartynski, R., Buhrman, A., Wojcik, L., Sievers, J., 1979. Metal/insulator composite selective absorbers. Sol. Energy Mater. 1, 105–124.

Janotti, A., Van de Walle, C.G., 2009. Fundamentals of zinc oxide as a semiconductor. Rep. Prog. Phys. 72, 1–29.

Kadirgan, F., Wackelgard, E., Söhmen, M., 1999. Electrochemical characterization of Al_2O_3–Ni thin film selective surface on aluminium. Turk. J. Chem. 23, 381–391.

Katumba, G.B., Mwakikunga, W., Mothibinyane, T.R., 2008. FTIR and Raman spectroscopy of carbon nanoparticles in SiO_2, ZnO and NiO matrices. Nanoscale Res. Lett. 3, 421–426.

Klochko, N.P., Volkova, N.D., Starikov, V.V., Kopach, V.R., Dobrotvorskaya, M.V., Mateychenko, P.V., Novikov, V.O., 2005. Utilization of alternating current methods for manufacture of selective absorbing coatings for heat collectors. Funct. Mater. 12, 548–554.

Klochko, N.P., Khrypunov, G.S., Myagchenko, Y.O., Melnychuk, E.E., Kopach, V.R., Klepikova, E.S., Lyubov, V.M., Kopach, A.V., 2012. Controlled growth of one-dimensional zinc oxide nanostructures in the pulsed electrodeposition mode. Semiconductors 46, 825–831.

Klochko, N.P., Khrypunov, G.S., Myagchenko, Y.O., Melnychuk, E.E., Kopach, V.R., Klepikova, E.S., Lyubov, V.M., Kopach, A.V., 2014. Electrodeposited zinc oxide arrays with the moth-eye effect. Semiconductors 48, 531–537.

Klochko, N.P., Klepikova, K.S., Khrypunov, G.S., Volkova, N.D., Kopach, V.R., Lyubov, V.M., Kirichenko, M.V., Kopach, A.V., 2015. Antireflective nanostructured zinc oxide arrays produced by pulsed electrodeposition. Fizika i Tekhnika Poluprovodnikov 49, 219–229.

Li, Z., Zhao, J., Ren, L., 2012. Aqueous solution-chemical derived Ni–Al_2O_3 solar selective absorbing coatings. Sol. Energy Mater. Sol. Cells 105, 90–95.

Mazda, F.F., 1987. Electronic Instruments and Measurement Techniques. Cambridge University Press, Cambridge.

Nuru, Z.Y., Arendse, C.J., Khamlich, S., Kotsedi, L., Maaza, M., 2014. A tantalum diffusion barrier layer to improve the thermal stability of Al_xO_y/Pt/Al_xO_y multilayer solar absorber. Sol. Energy 107, 89–96.

Nuru, Z.Y., Msimanga, M., Muller, T.F.G., Arendse, C.J., Mtshali, C., Maaza, M., 2015. Microstructural, optical properties and thermal stability of MgO/Zr/MgO multilayered selective solar absorber coatings. Sol. Energy 111, 357–363.

Palatnik, L.S., 1983. The Structure and Physical Properties of Solids. Laboratory Manual, The School-Book, Vishcha Shkola, Kiev.

Prasada Rao, T., Santhoshkumar, M.C., 2009. Effect of thickness on structural, optical and electrical properties of nanostructured ZnO thin films by spray pyrolysis. Appl. Surf. Sci. 255, 4579–4584.

Skompska, M., Zarębska, K., 2014. Electrodeposition of ZnO nanorod arrays on transparent conducting substrates – a review. Electrochim. Acta 127, 467–488.

Sokol, E.I., Tyukhov, I.I., Klochko, N.P., Khrypunov, G.S., Myagchenko, Y.O., Melnychuk, E.E., Kopach, V.R., Momotenko, O.V., Klepikova, K.S., Lyubov, V.M., Kopach, A.V., 2014. Pulse plating of semiconductors for solar cells. Sol. Energy 105, 373–380.

Tsybulya, S.V., Cherepanova, S.V., 2008. Introduction into Structural Analysis of Nanocrystals. Novosib. Gos Univ, Novosibirsk.

Yantara, N., Mathews, N., Jinesh, K.B., Kumar Mulmudi, H., Mhaisalkar, S.G., 2012. Modulating the optical and electrical properties of all metal oxide solar cells through nanostructuring and ultrathin interfacial layers. Electrochim. Acta 85, 486–491.

Zak, A.K., Majid, W.H.A., Abrishami, M.E., Yousefi, R., 2011. X-ray analysis of ZnO nanoparticles by Williamson–Hall and size–strain plot methods. Solid State Sci. 13, 251–256.